Streak Artifact Reduction in Human-scale Dark-field CT Using 3D Gaussian Splatting

T. Dorosti[*1,2,3], D. Frey[*1,2], J. B. Thalhammer[1,2,3,4], J. F. Hilmer[1,2], P. Bleuel[1,2], S. Peterhansl[1,2], J. McGinnis[5,6], D. Pfeiffer[3,4], F. Pfeiffer[1,2,3,4], D. Rueckert[5,6,7], F. Schaff[1,2]

***Abstract*—The clinical dark-field CT scanner (DFCT) enables attenuation- and small-angle scatter-based imaging of human-scale phantoms. Due to the scanner's vibrating Talbot-Lau grating interferometer, images suffer from inherent streak artifacts. In this work, DFCT data is processed by re-purposing the 3D Gaussian Splatting (3DGS) method, designed for rendering sparsely sampled X-ray attenuation data, and is compared against conventional filtering. A ventilated ex vivo porcine lung placed inside an anthropomorphic phantom was measured at 20 randomly selected table positions, and reconstructed with the filtered back-projection (FBP) algorithm at the clinical DFCT setup. The re-purposed 3DGS model was compared with Gaussian, bilateral, and total variation (TV) filters for post-processing DFCT data. For each conventional filter, the hyperparameters were optimized via grid search, maximizing the structural similarity index between 3DGS and the filtered image at the global image level. The contrast-to-noise ratio (CNR) and the full-width-at-half-maximum (FWHM) of manually-selected 20×20 pixel regions of lung tissue and air were calculated. The resulting mean and standard deviation values indicate that 3DGS outperforms conventional filtering in DFCT streak reduction, preserving edge sharpness and a high CNR, a necessity for diagnostic accuracy in future clinical trials.**

I. Introduction

Dark-field X-ray imaging is a technique sensitive to ultra-small-angle X-ray scattering of materials below the attenuation-based X-ray imaging spatial resolution, providing information about microstructures, such as pulmonary alveoli [1], [2]. With a Talbot–Lau interferometer, which consists of a set of periodic grating, attenuation, differential phase, and dark-field signals can be simultaneously measured [3]. Dark-field imaging has shown promising results in radiological applications, in particular as a complimentary functional imaging modality to X-ray attenuation-based radiography [4]–[6].

The Dark-field clinical CT scanner (DFCT) prototype at the Munich Institute of Biomedical Engineering allows for attenuation- and small-angle scatter-based imaging of human-scale phantoms. The system includes a vibrating Talbot–Lau grating setup embedded in the CT gantry to obtain the phase stepping values, as opposed to a discrete translational grating movement [7]. This clinical design choice challenges phase retrieval for DFCT reconstruction as it groups neighboring projection frames within a single gantry rotation to estimate the phase information, resulting in incomplete angular sampling for each reconstructed volume and leading to sparsely sampled streaking artifacts [8].

With a so-called multi-rotation scan, phase information is no longer sparsely sampled as multiple gantry rotations are acquired and utilized for phase retrieval and reconstruction of a single CT volume. Although multi-rotation scans come at the cost of increased acquisition time and radiation dose, limiting factors for practicality in clinical settings, they allow for DFCT processing and reconstructions with improved image quality and reduced streak artifacts [9].

Data-driven reconstruction and post-processing methods have been explored to tackle these limitations. Namely, convolutional neural networks have been shown to successfully reduce such streaks by learning a supervised mapping from single- to multi-rotation data [10]. While this method improves image quality, it depends on availability of high-quality ground truth (GT) multi-rotation data, which itself is affected by residual artifacts. Another limitation is posed by the domain gap between phantom data used for training and real-world clinical scans, which can hinder generalization.

Recently, self-supervised learning has gained popularity due to its domain-independent nature. Representation learning proposes alternative approaches to encoding image information, for example by replacing discrete voxels with parameterized Gaussians. Inspired by concepts from photogrammetry, 3D Gaussian splatting (3DGS) has emerged as a rendering technique capable of representing inconsistently sampled scenes [11].

The self-supervised approach of 3D R^2-Gaussian splatting has shown promise in reconstructing sparsely sampled X-ray data [12], effectively reducing streaking artifacts while preserving contrast and edge sharpness. By forward-projecting existing CT volumes and then reconstructing them with 3DGS, we effectively employ 3DGS as a post-processing step. In this work, we apply the 3DGS method to multi-rotation DFCT data and compare the results with those obtained using traditional post-processing filters. This aims at enhancing DFCT image quality to provide improved surrogate GT for supervised learning approaches.

II. Methods

A. Dataset

A ventilated ex vivo porcine lung placed inside an anthropomorphic Lungman phantom (Kyoto Kagaku, Tokyo, Japan)

*Equal contribution.

No live experiments were performed. Ethical approval was not required.

The authors declare no conflicts of interest.

[1]Chair of Biomedical Physics, Technical University of Munich (TUM), Germany
[2]Munich Institute of Biomedical Engineering, TUM, Germany
[3]Institute for Diagnostic and Interventional Radiology, TUM University Hospital, TUM, Germany
[4]TUM Institute for Advanced Study, TUM, Germany
[5]Chair for AI in Healthcare and Medicine, TUM, Germany
[6]Munich Center for Machine Learning (MCML), TUM, Germany
[7]Department of Computing, Imperial College London, U.K.

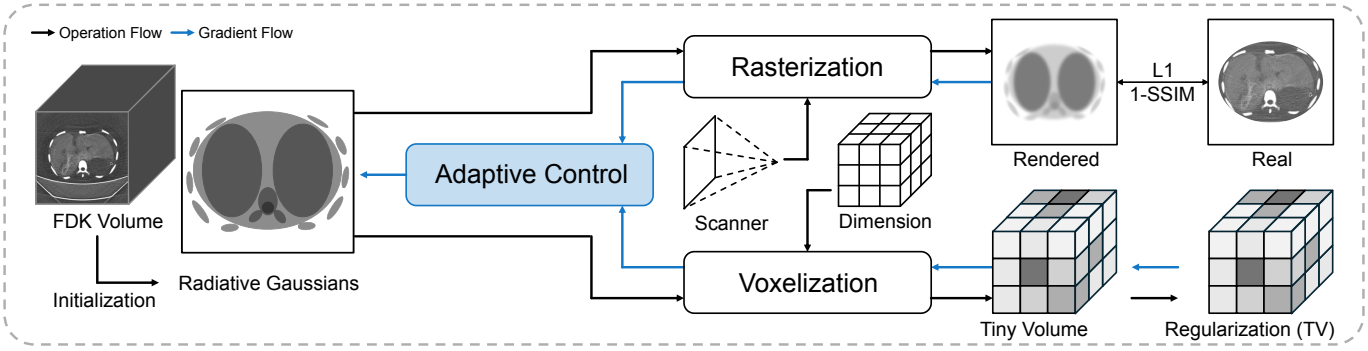

Fig. 1: Pipeline for the 3D Gaussian Splatting post-processing method for X-ray dark-field CT data. The volume is first rasterized with a differentiable renderer, computing pixel-wise projections through integration of the sum of 3D Gaussian density kernels along the X-ray path. Transformed ray-space 2D Gaussian kernels are used to calculate the L_1 and structural similarity index (SSIM) composite loss. The differentiable voxelizer tiles the 3D volume to accumulate neighboring radiative Gaussian contributions for total variation (TV) regularization of the discrete density volumes. Throughout the training process, the Gaussian density representations are dynamically adjusted with the adaptive control, such that important representations are densified, and others are removed. The pipeline is adapted from [12].

was measured at 20 randomly selected patient table positions. CT acquisitions were performed at $80\,\mathrm{kVp}$ and $550\,\mathrm{mA}$ at $1.5\,\mathrm{s}$ rotation time, with 2400 shots per revolution. The lung was ventilated at $10\,\mathrm{mbar}$. Multi-rotation scans (up to 20) were reconstructed from the full stack of recordings using virtual phase-stepping for phase retrieval and the filtered back-projection (FBP) algorithm onto a 800×800 pixel image matrix in the axial plane [9]. The multi-rotation acquisition increases the effective angular sampling for each reconstructed volume, thereby reducing streak artifacts at the expense of increased radiation dose.

B. Conventional Filtering

Streak reduction via post-processing with conventional filters was investigated to determine whether the same effect can be achieved by classical means. Namely, Gaussian, bilateral, and total variation (TV) filters were explored. For each conventional filter, the hyperparameters were optimized on the global axial slice level through a grid search to maximize the structural similarity index (SSIM) and peak signal-to-noise ratio (PSNR) between the proposed method (3DGS) and the conventional post-processing filtering methods. The resulting finalized hyperparameters and corresponding metrics are provided in Table I. Filters were implemented with Python's (version 3.12.10) Scikit-learn library (version 0.25.2).

TABLE I: Image-Level Comparison of 3DGS with Conventional Post-processing Filtering Methods ($n = 20$, mean $\pm$ std)

Metric	Gaussian	Bilateral	TV
SSIM	0.93 ± 0.02	0.96 ± 0.01	0.97 ± 0.02
PSNR (dB)	39.06 ± 0.92	39.47 ± 1.01	40.50 ± 0.82
Parameter	$\sigma = 1.00$	$\sigma_{Spatial} = 5.60$	$\lambda = 0.04$

C. 3D Gaussian Splatting

The 3DGS model from [12] was adapted and applied as post-processing to the DFCT data, as depicted in Fig. 1. First, all the data were normalized to a range of zero to one and zero-padded to include 800 axial slices, resulting in a final shape of $800 \times 800 \times 800$ pixels. Next, the 3DGS model was trained using the Tomographic Iterative GPU-based Reconstruction Toolbox (TIGRE version 3.0.0). Training took 75 minutes on an NVIDIA A100 GPU with $80\,\mathrm{GB}$ of VRAM for each volume. With fewer iterations and smaller volume sizes, training time can be substantially reduced.

Gaussian point clouds were initialized with the Feldkamp–Davis–Kress (FDK) algorithm. Throughout training, adaptive control was adjusted such that Gaussians with a size larger than $0.05\,\%$ of the volume were densified from the initial iteration onward, and those with density smaller than $1 \cdot 10^{-5}$ were pruned. Each volume was trained for a total of $30\,\mathrm{k}$ iterations with the Adam optimizer. Position, density, scale, and rotation learning rates were initially set to $2 \cdot 10^{-4}$, $1 \cdot 10^{-2}$, $5 \cdot 10^{-3}$, and $1 \cdot 10^{-3}$, respectively, and exponentially decayed at a rate of 0.1. The composite loss $\mathcal{L}_{total} = \mathcal{L}_1 + \lambda_{SSIM}(1 - \mathcal{L}_{SSIM}) + \lambda_{TV}\mathcal{L}_{TV}$ was utilized such that $\lambda_{SSIM} = 0.25$ and $\lambda_{TV} = 0.05$. The TV regularization volume size was set to 32 voxels. Optimization, learning rate, and loss parameters were unchanged from the values reported in [12], as additional grid-search fine-tuning of the control parameters did not improve training.

D. Evaluation Metrics

20×20 pixel regions of interest for lung tissue and air were manually selected for all scans. The mean and standard deviation of the contrast-to-noise ratio (CNR) and the full-width-at-half-maximum (FWHM) of the tissue-to-air edge spread function derivative were calculated as measures of contrast and sharpness, respectively.

III. Results

Evaluation of contrast (CNR) and sharpness (FWHM in pixels) over all samples is provided in Table II. Although the

TV filter results in a higher CNR in comparison to the 3DGS method ($CNR_{TV} = 8.09 \pm 3.47$, $CNR_{3DGS} = 6.74 \pm 2.51$), the comparative sharpness preserved with the 3DGS method is noticeable ($FWHM_{TV} = 15.80 \pm 16.21$, $FWHM_{3DGS} = 10.06 \pm 8.83$).

A comparison of all methods is also visualized with an example axial slice in Fig. 2. The lung tissue and air regions depicted allow for both qualitative and quantitative comparison of the dark-field signal contrast and sharpness between the two material edges. Gaussian and bilateral filters show poor performance for both CNR and FWHM, and the high CNR achieved by TV filtering is offset by over-smoothing at the lung tissue-air interface edge.

TABLE II: 20×20 Pixel Region-of-interest Comparison for Lung Tissue-to-Air Contrast and Sharpness Metrics with Various Post-processing Methods ($n = 20$, mean $\pm$ std)

Method	**CNR** ↑	**FWHM** ↓
Reference	2.44 ± 0.93	40.25 ± 11.32
Gaussian Filter	4.14 ± 1.48	31.99 ± 16.22
Bilateral Filter	6.44 ± 2.60	23.36 ± 16.33
TV Filter	8.09 ± 3.47	15.80 ± 16.21
3DGS	6.74 ± 2.51	10.06 ± 8.83

IV. Discussions and Outlook

The results suggest the potential of utilizing the 3DGS method for direct streak-free reconstruction of single-rotation DFCT data. Unlike the suggested 3DGS post-processing method, providing the raw projection data to the model ensures that no inherent FDK-reconstructed streaks will be forward-projected, further enhancing the CNR and FWHM for DFCT. However, a direct reconstruction of DFCT data using the 3DGS method is currently challenged by the intricate dark-field signal processing and phase retrieval of single-rotation data.

Applications of 3DGS for both post-processing and direct reconstruction of DFCT data, as well as the lack of domain constraints given the method's unsupervised nature, highlight its versatility and value. The proposed 3DGS post-processing explored in this work can be applied to further improve reference multi-rotation DFCT data, which is valuable for streak reduction in clinically relevant single-rotation DFCT scans within the supervised-learning approach introduced in [10].

The importance of dark-field image quality for diagnostic purposes is prevalent in the context of prospective clinical trials. To this end, future work should also validate the quality control and assessment of the various processing methods discussed in a clinically oriented reader study. Additionally, the 3DGS method is tailored for attenuation-based X-ray CT, and a fine-tuned adaptation of the proposed method to the dark-field imaging physics and CT processing should be investigated in more detail.

V. Conclusion

In this work, we compared post-processing of DFCT volumes with various conventional filtering and 3DGS methods.

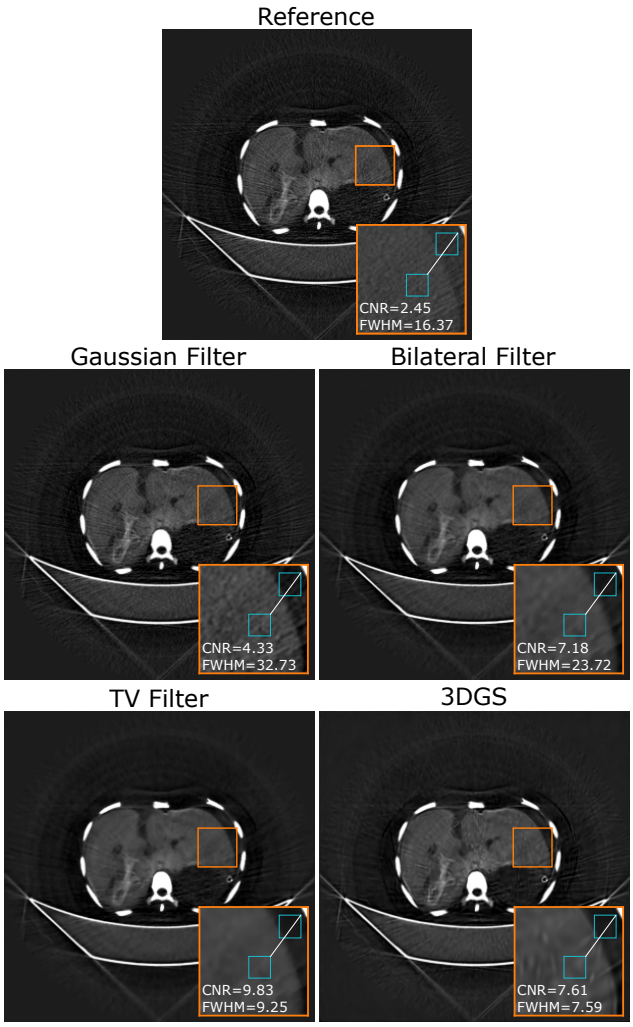

Fig. 2: Example axial DFCT slice, without (reference) and with streak-reduction post-processing. The contrast-to-noise ratio (CNR) and full-width-at-half-maximum (FWHM) values for the 20×20 pixel lung tissue and air regions (blue) are provided. The white line is used for pixel-wise FWHM calculation.

Our findings indicate that 3DGS outperforms conventional filtering in DFCT streak-reduction, preserving edge sharpness and a high CNR, a necessity for diagnostic accuracy in future clinical trials. While the study was limited to ex vivo phantom data, the findings suggest that 3DGS-based post-processing is a promising tool for improving DFCT image quality.

The availability of volumes reconstructed using classical methods, such as FBP, enables further extension of the proposed approach by fusing original and post-processed images, for example, via linear combination. In future work, enhanced 3DGS reconstructions could serve as improved GT for training supervised learning models.

Acknowledgment

Financial support through the European Research Council (ERC Smart Detectors for Darkfield X-ray Imaging, SyG

101167328), and the Free State of Bavaria under the Excellence Strategy of the Federal Government and the States, as well as by the Technical University of Munich – Institute for Advanced Study.

REFERENCES

[1] Pfeiffer, F., Bech, M., Bunk, O., Kraft, P., Eikenberry, E. F., Brönnimann, C., Grünzweig, C., and David, C., "Hard-x-ray dark-field imaging using a grating interferometer," *Nature Materials* **7**(2), 134–137 (2008).

[2] Bech, M., Jensen, T. H., Bunk, O., Donath, T., David, C., Weitkamp, T., Le Duc, G., Bravin, A., Cloetens, P., and Pfeiffer, F., "Advanced contrast modalities for x-ray radiology: Phase-contrast and dark-field imaging using a grating interferometer," *Zeitschrift Fur Medizinische Physik* **20**(1), 7–16 (2010).

[3] Pfeiffer, F., Weitkamp, T., Bunk, O., and David, C., "Phase retrieval and differential phase-contrast imaging with low-brilliance x-ray sources," *Nature Physics* **2**(4), 258–261 (2006).

[4] Urban, T., Gassert, F. T., Frank, M., Willer, K., Noichl, W., Buchberger, P., Schick, R. C., Koehler, T., Bodden, J. H., Fingerle, A. A., Sauter, A. P., Makowski, M. R., Pfeiffer, F., and Pfeiffer, D., "Qualitative and quantitative assessment of emphysema using dark-field chest radiography," *Radiology* **303**(1), 119–127 (2022).

[5] Urban, T., Sauter, A. P., Frank, M., Willer, K., Noichl, W., Bast, H., Schick, R., Herzen, J., Koehler, T., Gassert, F. T., Bodden, J. H., Fingerle, A. A., Gleich, B., Renger, B., Makowski, M. R., Pfeiffer, F., and Pfeiffer, D., "Dark-field chest radiography outperforms conventional chest radiography for the diagnosis and staging of pulmonary emphysema," *Investigative Radiology* **58**(11), 775–781 (2023).

[6] Gassert, F. T., Bast, H., Urban, T., Schick, R., Lochschmidt, M. E., Kaster, L., Koehler, T., Karrer, A., Keppler, A., Steinhardt, M., Marka, A. W., Steinhelfer, L., Sauter, A. P., Makowski, M. R., Pfeiffer, F., and Pfeiffer, D., "Dark-field chest radiography for pneumothorax detection: A prospective study," *Radiology. Cardiothoracic Imaging* **7**(6), e240560 (2025).

[7] Viermetz, M., Gustschin, N., Schmid, C., Haeusele, J., von Teuffenbach, M., Meyer, P., Bergner, F., Lasser, T., Proksa, R., Koehler, T., and Pfeiffer, F., "Dark-field computed tomography reaches the human scale," *Proceedings of the National Academy of Sciences* **119**(8), e2118799119 (2022). Publisher: Proceedings of the National Academy of Sciences.

[8] Schmid, C., Viermetz, M., Gustschin, N., Noichl, W., Haeusele, J., Lasser, T., Koehler, T., and Pfeiffer, F., "Modeling Vibrations of a Tiled Talbot-Lau Interferometer on a Clinical CT," *IEEE Transactions on Medical Imaging* **42**(3), 774–784 (2023).

[9] Haeusele, J., Schmid, C., Viermetz, M., Gustschin, N., Lasser, T., Koehler, T., and Pfeiffer, F., "Advanced phase-retrieval for stepping-free x-ray dark-field computed tomography," *IEEE Transactions on Medical Imaging* **42**(10), 2876–2885 (2023).

[10] Kumschier, T., Thalhammer, J., Schmid, C., Haeusele, J., Koehler, T., Pfeiffer, F., Lasser, T., and Schaff, F., "Streak artefact removal in x-ray dark-field computed tomography using a convolutional neural network," *Medical Physics* **51**(10), 7404–7414 (2024).

[11] Kerbl, B., Kopanas, G., Leimkuehler, T., and Drettakis, G., "3D Gaussian Splatting for Real-Time Radiance Field Rendering," *ACM Transactions on Graphics* **42**(4), 1–14 (2023).

[12] Zha, R., Lin, T. J., Cai, Y., Cao, J., Zhang, Y., and Li, H., "R²-gaussian: Rectifying radiative gaussian splatting for tomographic reconstruction," (2024).